ESC European Society of Cardiology

Cardiovascular Research (2025) **121**, 311–323
https://doi.org/10.1093/cvr/cvae258

Meis transcription factors regulate cardiac conduction system development and adult function

Noelia Muñoz-Martín[1], Ana Simon-Chica [2], Covadonga Díaz-Díaz [1], Vanessa Cadenas[1,3], Susana Temiño[1,3], Isaac Esteban [1], Andreas Ludwig[4], Barbara Schormair [5], Juliane Winkelmann[5], Veronika Olejnickova [6], David Sedmera [6], David Filgueiras-Rama [2,3,7], and Miguel Torres [1,3]*

[1]Cardiovascular Regeneration Program, Centro Nacional de Investigaciones Cardiovasculares (CNIC), 3 Melchor Fernández Almagro, Madrid 28029, Spain; [2]Novel Arrhythmogenic Mechanisms Program, Centro Nacional de Investigaciones Cardiovasculares (CNIC), 3 Melchor Fernández Almagro, Madrid 28029, Spain; [3]Centro de Investigación Biomédica en Red de Enfermedades Cardiovasculares (CIBERCV), 3-5 Av. Monforte de Lemos, Madrid 28029, Spain; [4]Institut für Experimentelle und Klinische Pharmakologie und Toxikologie, Friedrich-Alexander-Universität Erlangen-Nürnberg, 17 Fahrstraße, Erlangen 91054, Germany; [5]Institute of Neurogenomics, Helmholtz-Zentrum, 1 Ingolstädter Landstraße, Neuherberg 85764, Germany; [6]First Faculty of Medicine, Institute of Anatomy, Charles University, U Nemocnice 3, Praha 2, 128 00, Czech Republic; and [7]Instituto de Investigación Sanitaria del Hospital Clínico San Carlos (IdISSC), Calle del Prof Martín Lagos, Madrid 28040, Spain

Received 11 August 2022; revised 9 September 2024; accepted 1 October 2024; online publish-ahead-of-print 18 December 2024

Time for primary review: 27 days

Aims

The cardiac conduction system (CCS) is progressively specified during development by interactions among a discrete number of transcription factors (TFs) that ensure its proper patterning and the emergence of its functional properties. Meis genes encode homeodomain TFs with multiple roles in mammalian development. In humans, Meis genes associate with congenital cardiac malformations and alterations of cardiac electrical activity; however, the basis for these alterations has not been established. Here, we studied the role of Meis TFs in cardiomyocyte development and function during mouse development and adult life.

Methods and results

We studied *Meis1* and *Meis2* conditional deletion mouse models that allowed cardiomyocyte-specific elimination of Meis function during development and inducible elimination of Meis function in cardiomyocytes of the adult CCS. We studied cardiac anatomy, contractility, and conduction. We report that Meis factors are global regulators of cardiac conduction, with a predominant role in the CCS. While constitutive Meis deletion in cardiomyocytes led to congenital malformations of the arterial pole and atria, as well as defects in ventricular conduction, Meis elimination in cardiomyocytes of the adult CCS produced sinus node dysfunction and delayed atrio-ventricular conduction. Molecular analyses unravelled Meis-controlled molecular pathways associated with these defects. Finally, we studied in transgenic mice the activity of a *Meis1* human enhancer related to an single-nucleotide polymorphism (SNP) associated by Genome-wide association studies (GWAS) to PR (P and R waves of the electrocardiogram) elongation and found that the transgene drives expression in components of the atrio-ventricular conduction system.

Conclusion

Our study identifies Meis TFs as essential regulators of the establishment of cardiac conduction function during development and its maintenance during adult life. In addition, we generated animal models and identified molecular alterations that will ease the study of Meis-associated conduction defects and congenital malformations in humans.

Keywords

Cardiac development • PR elongation • Sinus node dysfunction • Transcription factor • Mouse targeted mutation

* Corresponding author. Tel: +34 914531200; fax: +34 914531265, E-mail: mtorres@cnic.es

1. Introduction

Meis transcription factors (TFs) belong to the three aminoacid loop extension family and are highly conserved in evolution at the molecular and functional levels.[1] *Meis1* (myeloid ecotropic viral integration site 1) was the first gene of the family to be identified.[2] In mammals, two additional highly similar genes have been identified; *Meis2* and *Meis3*.[3,4] Except in the head, the embryonic expression patterns of *Meis1* and *Meis2* are highly coincident and both genes encode very similar proteins with redundant functions.[5] In contrast, Meis3 expression is mainly restricted to the hindbrain, although it can be also detected in the heart, spleen, and lung at later stages.[4] Understanding Meis roles in cells in which Meis1 and Meis2 are co-expressed therefore involves the elimination of both genes.

Meis TFs function as co-factors of other TFs, such as Pbx, Prep, or Hox factors.[6] They can form dimers or trimers, modifying the co-factors' affinity and selectivity for DNA-binding sites. Thus, there is increased difficulty in understanding Meis TFs function, because it is highly context dependent. *Meis1* knockout mice die around E14.5 due to failing haematopoiesis.[7–9] Additional defects in *Meis1*-deficient embryos include eye hypoplasia, cardiac inter-ventricular septum (IVS) defects, and over-riding aorta.[7,9–11] *Meis2*-deficient mice also die around E14.5 and show haematopoietic defects and persistent truncus arteriosus.[12]

Meis TFs also play roles in post-natal life. *Meis1* is important for the maintenance of haematopoietic stem cell quiescence in the bone marrow haematopoietic niche.[13–15] In the post-natal heart, Meis1 is important for the cell cycle arrest that takes place after birth in mouse cardiomyocytes.[16] In humans, a rare germline heterozygous *Meis2* mutation is associated with palatal defects, intellectual disability, and congenital heart defects, including ventricular septal defect and over-riding aorta.[17–19] In addition, *Meis1* genetic variants are associated with PR (P and R waves of the electrocardiogram) elongation in humans, suggesting a Meis role in atrio-ventricular conduction.[20,21] These results indicate that Meis TFs are not only involved in human heart morphogenesis but also in the regulation of cardiomyocyte specialized functions; however, this aspect has not been explored in animal models.

Genetic analyses in mouse models have advanced our knowledge on the transcriptional control of cardiac conduction system (CCS) development. Members of the Tbx-, GATA-, and Irx-family, Isl1, Nkx2.5, Shox2, and other TFs have been found essential for the specification and regional specialization of the CCS (reviewed in the study by van Eif *et al.*[22]). In contrast, the study of the role of developmental transcriptional regulatory networks during the maintenance of CCS physiology in the adult heart has remained less studied.[23,24]

Here, we studied the roles of *Meis1* and *Meis2* in cardiomyocytes using genetic mouse models. We report that Meis TFs are required for cardiac conduction with a predominant role in the cardiomyocytes of the CCS, including the sinoatrial node (SAN) and the atrio-ventricular and ventricular conduction systems. Interestingly, Meis function is not only restricted to CCS development but also required for the maintenance of adult CCS physiology, including SAN pacemaker function and atrio-ventricular conduction. In particular, in the mouse models generated we observed elongation of the PR interval (time between P and R waves onset in the electrocardiogram), which reproduces the Genome-wide association studies (GWAS) association between *Meis1* and PR interval prolongation in humans. In addition, our study identifies congenital defects partially overlapping those reported in patients that carry *Meis2* mutations. Our study identifies Meis TFs as essential regulators of cardiac conduction development and adult physiology and provides animal models for *Meis*-associated conduction defects and congenital malformations.

2. Methods

2.1 Mouse strains

All animal procedures in the MT laboratory were approved by the CNIC Animal Experimentation Ethics Committee, by the Community of Madrid (Ref. PROEX 144.1/21), and conformed to EU Directive 2010/63EU and Recommendation 2007/526/EC regarding the protection of animals used for experimental and other scientific purposes, enforced in Spanish law under Real Decreto 1201/2005. In this study, mice were maintained on a mixed genetic background. Mice were euthanized by CO_2 inhalation according to the European Commission recommendations for the euthanasia of experimental animals.

Mouse lines used were *Meis1*^{ECFP} and *Meis1*^{CreER},[11] *R26R*^{TdTomato},[25] *Meis1*^{flox},[13] *Meis2*^{flox},[26] *α-MHC*^{Cre},[27] *Hcn4*^{CreERT2},[28] and *617-HCRE*.[29]

For the generation of M1M2KO mice, we crossed *Meis1*$^{flox/flox}$; *Meis2*$^{flox/flox}$ females with *Meis1*$^{flox/+}$; *Meis2*$^{flox/flox}$; *α-MHC*$^{Cre/+}$ males in order to obtain 25% of embryos with Meis1 and Meis2 double homozygous deletion. Animals resulting from the same crosses that did not inherit the Cre allele were used as controls.

For the generation of M1M2 CSiKO mice, we crossed *Meis1*$^{flox/flox}$; *Meis2*$^{flox/flox}$ females with *Meis1*$^{flox/+}$; *Meis2*$^{flox/flox}$; *Hcn4*$^{CreERT2/+}$ males in order to obtain 25% of embryos with Meis1 and Meis2 double homozygous deletion in the conduction system following tamoxifen exposure. Animals resulting from the same crosses that did not inherit the CreERT2 allele were used as controls. For experiments, all animals received the same tamoxifen dose, as described below.

2.2 Tamoxifen administration

Two hundred milligrams of tamoxifen (Sigma-T5648-1G) were dissolved in 20 mL of corn oil (Sigma-C8267) for a final concentration of 10 mg/mL. A daily dose of 100 µL from this solution was administered by oral gavage to adult mice for five consecutive days.

2.3 Immunofluorescence

Hearts dissected and fixed overnight at 4°C in 2% paraformaldehyde in phosphate buffered saline (PBS) and whole/mount stained or embedded in gelatine or paraffin for sectioning. Primary antibodies used were anti-Meisa (1:500),[30] anti-Meis2 (1:500),[30] cTnT (1:200, MS-295 Thermo Scientific), Cx43 (1:200, Sigma C6219), green fluorescent protein (GFP) (1:200, Acris R1091P), Hcn4 (1:100, Abcam ab85023 and 1:200 Sigma-Aldrich AB5808), Cx40 (1:200, Invitrogen 378900), and Scn5a (1:200, Alomone Labs ASC-005). Cryosections or paraffin sections were permeabilized with PBT (PBS with 0.5% Triton X-100) and blocked with universal Tris/NaCl/blocking reagent (TNB) FP1012-Perkin Elmer. Primary antibodies were incubated at 4°C overnight and secondary antibodies for 1 h at room temperature. Secondary antibodies were anti-rabbit Alexa633 and 594 (Life Technologies A21071 and A11012), anti-rabbit-horseradish peroxidase (HRP) (Dako P0448), anti-mouse Alexa488 (Life Technologies A11029), and anti-goat-biotin (Jackson 705-065-003) all at 1:500 concentration. Sections were mounted using Dako fluorescence mounting medium (s3023). Whole-mount atria were stained with wheat germ agglutinin (WGA-Thermo Scientific-W21404) and optically cleared using Abberior TDE Mounting Medium.

2.4 *In situ* hybridization on sections

Paraffin sections were rehydrated from xylol to PBS passing through sterile solutions with decreasing concentrations of ethanol. Sections were digested with proteinase K (10 µg/mL) at 37°C for 10 min. Riboprobe hybridization was performed at 65°C overnight. The next day, sections were washed and incubated with anti-DIG antibody at 4°C overnight. Then, sections were developed with BM-purple (Roche, ref 11442074001) at room temperature or 37°C. Time of development was about 5 days.

2.5 Image acquisition and analysis

Images of the *in situ* hybridization were acquired with a Nikon Eclipse 90i microscope. H&E and Sirius Red stained sections were scanned with Hamamatsu Nanozoomer 2.0 RS and NDP.Scan 2.5 software. Analysis and quantifications were performed with the NDP Analyzer software.

Immunofluorescence images were acquired with a Zeiss LSM 700 confocal microscope using 405, 458, 488, 568, and 633 nm wavelengths and ×10/0.45 dry, ×25×\/0.8, and ×40/1.3 oil objectives. Whole-mount atria 3D images were obtained with the Leica TCS SP8 coupled to a DMi8 inverted confocal microscope Navigator module equipped with light laser. Z-stacks were captured every 4 µm using a ×10/0.4 dry objective. To estimate ploidy in isolated cardiomyocytes, nuclear volumes and 4′,6-diamidino-2-phenylindole (DAPI) intensity were measured with acquired confocal z-stacks at high magnification (×63/1.4 oil) with 2 µm Z-steps using a Zeiss LSM 700 confocal microscope. Image J (https://imagej.nih.gov/ij/) was used for image analysis.

2.6 Echocardiography

For pre-natal echocardiography, pregnant females were anaesthetized with 2% isofluorane in oxygen. Abdominal surgery was then performed for uterus exposure. After surgery, isoflurane was adjusted to maintain a heart rate at 450 ± 50 b.p.m., and foetuses were exposed one at a time to keep them as warm as possible. An infra-red heat lamp was used for the same purpose during acquisition. Echocardiography was performed by an expert operator using a high-frequency ultrasound system (Vevo 2100, Visualsonics, Toronto, ON, Canada) with a 50 MHz probe on a heating platform. Bidimensional (2D), M-Mode echocardiography was used to visualize the hearts in long-axis and short-axis (SAX) views. Left and right ventricular ejection fractions (EFs), wall thickness, and diastolic and systolic chamber dimensions were assessed from the M-Mode SAX view. EF was calculated from the SAX view at the level of the papillary muscles and using the Teichholz method.[31] Heart rate was calculated using three consecutive outflow waves. Corrected ventricular masses were calculated from M-mode images according to the following formula for the left ventricle (LV): $1.053 \times [(\mathrm{LVIDd} + \mathrm{LVPWd} + \mathrm{VSTd})^3 - (\mathrm{LVIDd})^3] \times 0.8$, where LVIDd, diastolic LV inner dimension; LVPW, diastolic LV posterior wall thickness, and VSTd, ventricular septum thickness. The procedure for right ventricular (RV) mass estimation was similar, taking into account that before birth both ventricles are rather similar and both serve the systemic circulation. The position of the foetuses was recorded, so that foetal identity could be tracked for genotyping. This procedure was therefore blinded to the genotype of the foetuses. A similar procedure was performed for adult mouse heart echography without surgery.

2.7 Optical mapping

Pregnant females at ED14.5 or ED16.5 were sacrificed by cervical dislocation, and the embryos were harvested. Heart isolation from the embryos was performed in a Petri dish with ice-cold Tyrode's Buffer to prevent ischaemic damage. Harvested hearts were placed in wells of a P12 dish on ice and incubated for 15 min in 500 µL of ice-cold Tyrode's Buffer with 25 µL of di-4-ANEPPS (stock solution in Dimethyl sulfoxide [DMSO], 1.25 mg/mL, Invitrogen [Waltham, Massachusetts, United States]) and 2 µL of blebbistatin (14 mM stock in DMSO, Sigma [Burlington, Massachusetts, United States]) in darkness. After staining, hearts were pinned in a custom-made heated dish (37°C) with continuously oxygenated Tyrode's Buffer with 14 µM blebbistatin. Membrane voltage changes were recorded as fluorescence changes over time at 1 kHz from both anterior and posterior aspects of the heart using Ultima L high-speed camera (SciMedia, Japan), and bundled software (BV_Analyzer) was used to generate epicardial activation maps as described.[32]

2.8 Electrocardiogram

Electrocardiogram (ECG) recordings were obtained in sedated animals as reported elsewhere.[33] Briefly, mice were anaesthetized with 1.5% isoflurane in oxygen, inhaled through a facial mask. To avoid night-day circadian variations, ECGs were performed in the morning. Expert operators (V.C. and S.T.) gently handled the animals to insert subcutaneously ECG electrodes in the terminal end of the four limbs. Additional ECG gel was used to improve signal-to-noise ratio. Then, ECG recordings were acquired for 60 s at 2 kHz sweep speed using a MP36R data acquisition workstation (Biopac Systems). Data were stored for off-line analysis using custom MatLab scripts for pre-processing, visualization, and quantification of electrophysiological intervals and heart rate[34] (see Supplementary material online, *Figure S1*).

After band-pass filtering between 0.5 and 200 Hz, baseline wander was removed using a bidirectional filtering strategy. We removed and excluded ECG segments with noise artefacts manually using sequential previsualization of 10 s segments. To detect the R-peak of the QRS complex (green dots in Supplementary material online, *Figure S1*), we used parabolic fitting of the Coiflet wavelet transformation and further detection of the maximum magnitude point. All R-peak detections were supervised to ensure accuracy of ECG segmentations. After detection of the QRS complex, P- and T-waves and ECG intervals were extracted using adaptive windowing depending on beat-to-beat R–R changes. More specifically: (i) PR intervals were measured from the beginning of the P-wave to the beginning of the R-wave/Q-wave; (ii) QRS intervals were measured from the beginning of the Q-wave until the point where the S-wave crosses the baseline; and (iii) QT intervals were measured from the beginning of the Q-wave until the point where the T-wave declines to 90% (T90) from the peak. Adaptive heart rate–corrected QT values were derived using a modification of Bazett's formula for murine electrocardiography.[35] From the evaluation of control mice at 2 and 6 months of age, we established a sub-domain of normal RR (time between two consecutive R waves onset in the electrocardiogram) variability among all ECG traces. Then, we defined the presence of sinus node dysfunction when the animal-specific RRn + 1 vs. RRn (correlation between the duration of consecutive RR intervals) domain fell partially or completely out of the normal RR variability sub-domain identified in controls. Dimensionless RR intervals were also plotted over the 60 s electrogram recordings to detect sinus rhythm alterations. A free copy of the custom-made ECG tool for semi-automatic analysis of large amounts of data from long-duration ECG recordings in mice can be obtained from D.F.-R. upon request.

2.9 RNA sequencing

Four control and four M1M2DKO foetuses were harvested at E15.5 from four independent litters. Hearts were dissected in ice-cold sterile PBS. Atria and ventricles were separated and outflow tract (OFT) removed. Then, atria and ventricles were separated and all other tissues were removed. Tissue lysis was performed with TissueLyser LT (Quiagen [Germantown, Maryland, United States]) or TriReagent (Trizol, Sigma-T9424) and RNA isolation with RNeasy Mini or Midi Kit (Quiagen) for embryonic and adult tissues, respectively. Library and sequencing were performed at CNIC Genomic Unit. Twenty nanograms of total RNA were used to generate barcoded RNA-seq libraries using the NEBNext Ultra RNA Library preparation kit (New England Biolabs [Ipswich, Massachusetts, United States]). The size and the concentration of the libraries were checked using the TapeStation 2200 DNA 1000 chip. Libraries were sequenced on a HiSeq2500 (Illumina, San Diego, California, United States) to generate 60-base single reads. FastQ files for each sample were obtained using bcltofastQ software 2.20. Gene Set Enrichment Analysis was performed with genes differentially expressed using the Broad Institute GSEA 'Molecular Signatures Database' computing overlaps with Kyoto Encyclopedia of Genes and Genomes (KEGG) and Gene Ontology gene sets. RNA-seq data are available from the GEO database with accession number GSE213356.

2.10 Bioinformatic analysis

Public Meis1 ChIP-seq data[36] were integrated with available ATAC-seq data from right atrial Cardiomyocytes (CMs) and pacemaker CMs.[37] Raw ATAC-seq sequencing data were processed in order to obtain a list of accessible DNA regions. Adapters were trimmed using Cutadapt v.1.7.1,[38] and reads were mapped against mouse mm10 reference genome using bowtie2 v.2.2.5.[39] Duplicated sequences were annotated with Markduplicates v.1.97 from the 'Picard Tools', Broad Institute GitHub repository (http://broadinstitute.github.io/picard/). Unmapped sequences, secondary alignments, and low-quality reads were filtered out. Peaks

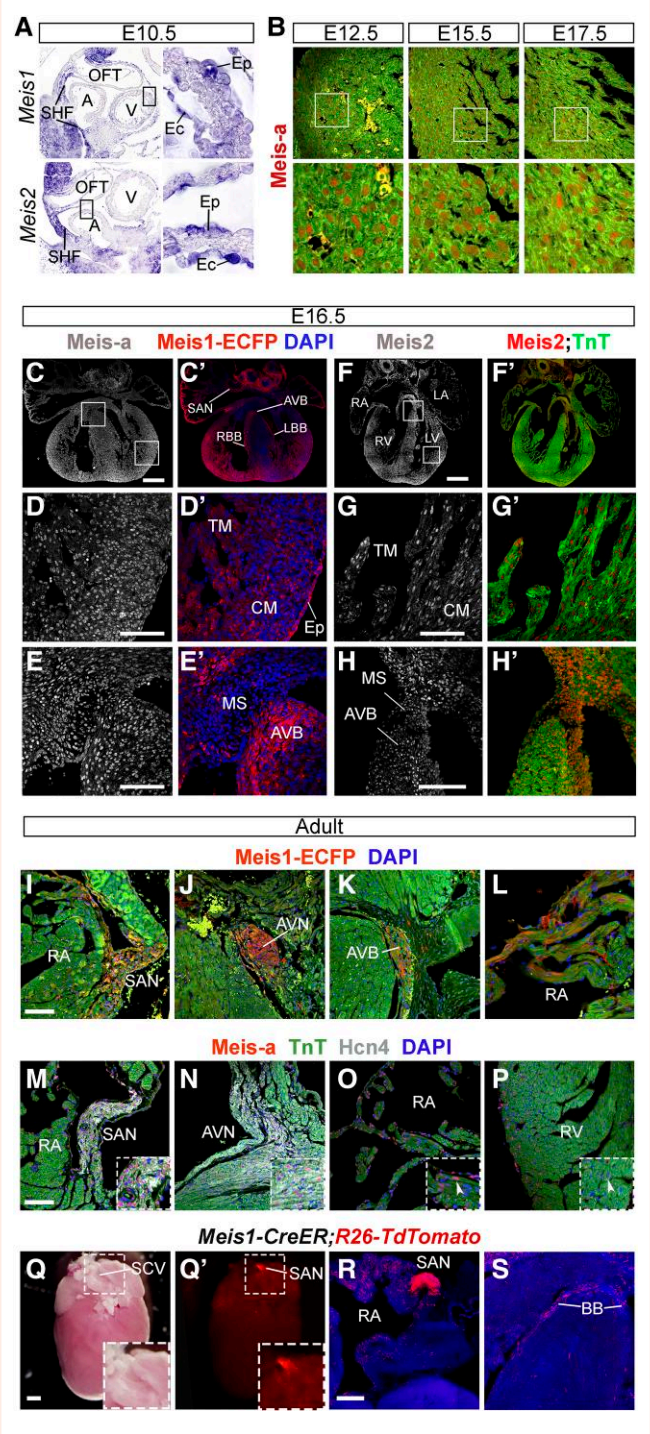

Figure 1 Expression of Meis1 and Meis2 in the developing and adult heart. (*A*) *Meis1* and *Meis2* mRNA *in situ* hybridization showing expression in the second heart field, pericardium, endocardium (Ec), and epicardium (Ep) at E10.5. Boxed regions indicate magnifications shown in the panels to the right side. (*B*) Confocal images of ventricles at the indicated embryonic days showing anti-Meisa immunofluorescence. Boxed areas are magnified in the panels below. (*C–E'*) Confocal images from sections of E16.5 hearts with the *Meis1*^{ECFP} line combined with anti-Meisa. (*F–H'*) Confocal images from sections of E16.5 hearts showing anti-Meis2 and anti-cTNT immunofluorescence. Boxes in (*C*) and (*F*) indicate magnified regions in (*D* and *E'*) and (*G* and *H'*). (*I–L*) Confocal images showing the distribution

(continued)

Figure 1 Continued

of ECFP in the CCS and atrial myocardium of *Meis1*^{ECFP} adult hearts. (*M–P*) Anti-Meisa and anti-Hcn4 immunofluorescence in the SAN (*M*) and AVN (*N*), RA (*O*), and ventricular CMs (*P*). Dotted lines indicate magnified areas, and arrowheads within show anti-Meisa-positive CMs. (*Q* and *Q'*) Whole-mount brightfield and fluorescent confocal images of *Meis1*^{CreER}; *R26R*^{TdTomato} adult hearts showing strong recombination in the SAN following tamoxifen administration. Tamoxifen was administered by oral gavage to 10 weeks old mice at a dose of 1 mg/day for five consecutive days. Hearts were harvested 2 days after tamoxifen administration. (*R* and *S*) Two hundred micrometer-*thick sections of the same heart, stained with DAPI and acquired by confocal microscopy* (maximum projection). (*R*) Shows expression in RA and SAN and (*S*) expression in the BBs. Scale bars: 100 μm, except in (*Q*) (1 mm) and (*R*) (300 μm). CM, ventricular compact myocardium; TM, trabecular myocardium; MS, membranous septum; V, ventricle; M, myocardium; LA, left atrium; RBB, right BB; LBB, left BB.

were called using MACS2 v.2.2.9.1[40] callpeaks function with the parameters --nomodel --shift -100 --extsize 200 commonly used for ATAC-seq data. Overlapping peaks between ChIP-seq and ATAC-seq data were obtained using the GenomicRanges[41] package in R. ATAC reads inside Meis1 peaks were quantified using the samtools v.0.1.18[42] bedcov function and normalized by mapped library size.

2.11 Statistical analysis

All statistical analyses are detailed in the figure legends.

3. Results

3.1 Meis1 and Meis2 expressions in the developing and adult mouse heart

To characterize Meis function in cardiomyocytes, we studied the expressions of *Meis1* and *Meis2* in the developing and adult mouse heart. In the embryonic heart, up to embryonic day of development 10.5 (E10.5), *Meis1* and *Meis2* mRNA expressions were detected in the second heart field, epicardium, and endocardium, but not in the heart tube, indicating that Meis TFs associate at these early stages with a cardiac progenitor phenotype (*Figure 1A*). In contrast, from mid-gestation towards birth, Meis proteins revealed with a pan-Meis antibody were detected in differentiating cardiomyocytes (*Figure 1B–E*). Specific detection of *Meis1* expression using an ECFP knock-in reporter[11] showed at mid-gestation strong expression in the SAN, atrio-ventricular bundle (AVB), trabecular myocardium, and atrial myocardium (*Figure 1C'–E'*). Lower expression levels were detected in the ventricular working myocardium (*Figure 1D'*). Specific detection of Meis2 showed generalized expression in cardiomyocytes, with higher expression in the AVB (*Figure 1F–H'*). In the adult heart, both the *Meis1* reporter and the pan-Meis antibody showed a strong signal the SAN, atrio-ventricular node (AVN), and AVB (*Figure 1I–K*, *M*, and *N*), a lower level of expression in atrial cardiomyocytes (*Figure 1L–O*) and very low expression in ventricular working cardiomyocytes (*Figure 1P*). Consistent with these results, tracing *Meis1*-expressing cells using knock-in *Meis1*^{CreERT2} tracer line showed high density of labelled cells in the SAN, a medium density in atria and the bundle branches (BBs), and very low density in the working myocardium (*Figure 1Q–S*).

3.2 Characterization of *Meis1* and *Meis2* functions in cardiomyocytes

To study the function of Meis TF in cardiomyocytes, we recombined floxed *Meis1* and *Meis2* alleles with *αMHC-Cre*, generating double *Meis1* and *Meis2* disruption in cardiomyocytes (M1M2DKO; *Figure 2A* and *B*). We did not

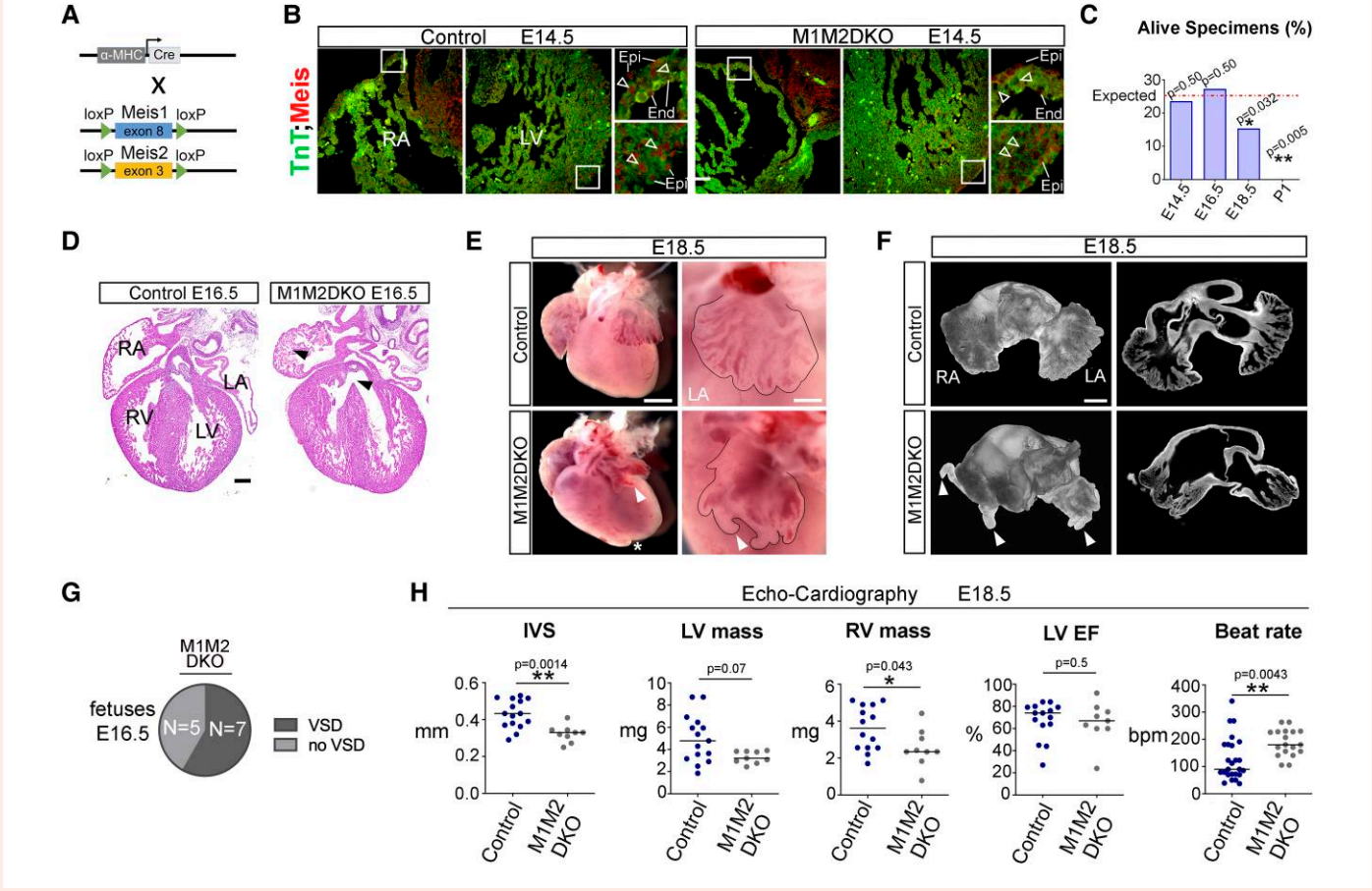

Figure 2 Anatomical and functional consequences of the elimination of *Meis1* and *Meis2* function in cardiomyocytes during embryonic development. (*A*) Model for simultaneous constitutive deletion of *Meis1* and *Meis2* in CMs. (*B*) Confocal images of control and M1M2DKO embryos showing the loss of Meis expression in mutant cardiomyocytes by immunofluorescence with anti-Meisa and cTNT. Boxes indicate the magnified regions shown in the panels on the right side. Arrowheads point to cardiomyocyte nuclei with or without Meis expression. Scale bars: 100 µm. (*C*) Expected and observed frequencies of M1M2DKO foetuses at different embryonic days. E.14.5 $n = 72$; E16.5 $n = 66$; E18.5 $n = 130$; P1 $n = 27$. One-tailed Fisher's test. (*D*) Four-chamber view of E16.5 control and mutant embryonic heart sections stained with H&E. Arrowheads point to VSD and RA morphology. Scale bar: 200 µm. (*E*) Ventral view of representative whole-mount E18.5 hearts from control and mutant littermates. Arrowhead points to finger-like projections in the left atrium. Scale bar: 500 µm. Panels on the right side show magnification of left atria for better appreciation of the altered morphology. Scale bar: 200 µm. (*F*) Three-dimensional reconstruction of whole-mount confocal images from E18.5 control and mutant atria stained with WGA. Arrowheads indicate finger-like projections in the mutant atrium. Panels on the right side show individual confocal sections the reconstructed specimens. Scale bar: 400 µm. (*G*) Classification of M1M2DKO fetuses at E16.5 according to the presence of VSD, $n = 12$. (*H*) Results from transuterine echocardiography of control and mutant foetuses at 18.5. $n = 15$ control and 9 mutant specimens for all graphs except for bmp, in which 26 control and 18 mutant specimens were used. LV and RV masses were corrected. Unpaired two-tailed Mann–Whitney test. Lines show the mean and dots, individual measurements on different specimens.

recover any live M1M2DKO animal at post-natal Day 1 (P1), while 60% were found alive at E18.5 (*Figure 2C*), indicating that most deaths took place at the end of gestation or perinatally. Anatomically, mutant hearts showed ventricular septum defect (VSD), with inter-ventricular communication (60% of mutants) and over-riding aorta (80% of hearts with VSD; *Figure 2D* and *G*). In addition, atria were strongly dysmorphic, showing hypoplasia and finger-like protrusions (*Figure 2F*). Evaluation of IVS thickness and ventricular mass by echocardiography at E18.5 (*Figure 2H*) suggested mild hypoplasia of mutant hearts, while LV function was preserved. Mutant hearts at E18.5 showed a higher beat rate than control hearts, suggesting alterations of the SAN.

We then studied by RNA-seq how the elimination of Meis function affects the cardiomyocyte molecular profile. For this, we separately analysed the atria and ventricles of E15.5 M1M2DKO hearts. We found a high number of differentially expressed genes between mutants and controls in E15.5 atria and a lower number in ventricles at E15.5 (*Figure 3A*; see Supplementary material online, *Datasets S1* and *S2*). This observation matches the expression profile of Meis genes and the strong dysmorphology of the atria in M1M2DKO hearts.

Pathway analysis of the differentially expressed genes (*Figure 3B* and *C*) identified an association with pathological conditions like arrhythmogenic RV cardiomyopathy, hypertrophic cardiomyopathy, and dilated cardiomyopathy. In relation to biological processes, 'cardiac contraction' and 'calcium signalling' were detected. The most prominent molecular pathways detected related to 'GAP junction', 'focal adhesion', 'Extra-cellular matrix (ECM)-receptor interaction,' and 'Wnt signalling', suggesting the cell–cell and cell–ECM interactions, were the most affected pathways.

To determine the validity of this analysis, we studied whether the differentially expressed genes were enriched for Meis1/2-bound genes, comparing our data with previously reported ChIP-seq data[36] that identified the distribution of Meis protein binding in the chromatin. We found a significant association between the genes differentially repressed or activated upon Meis inactivation

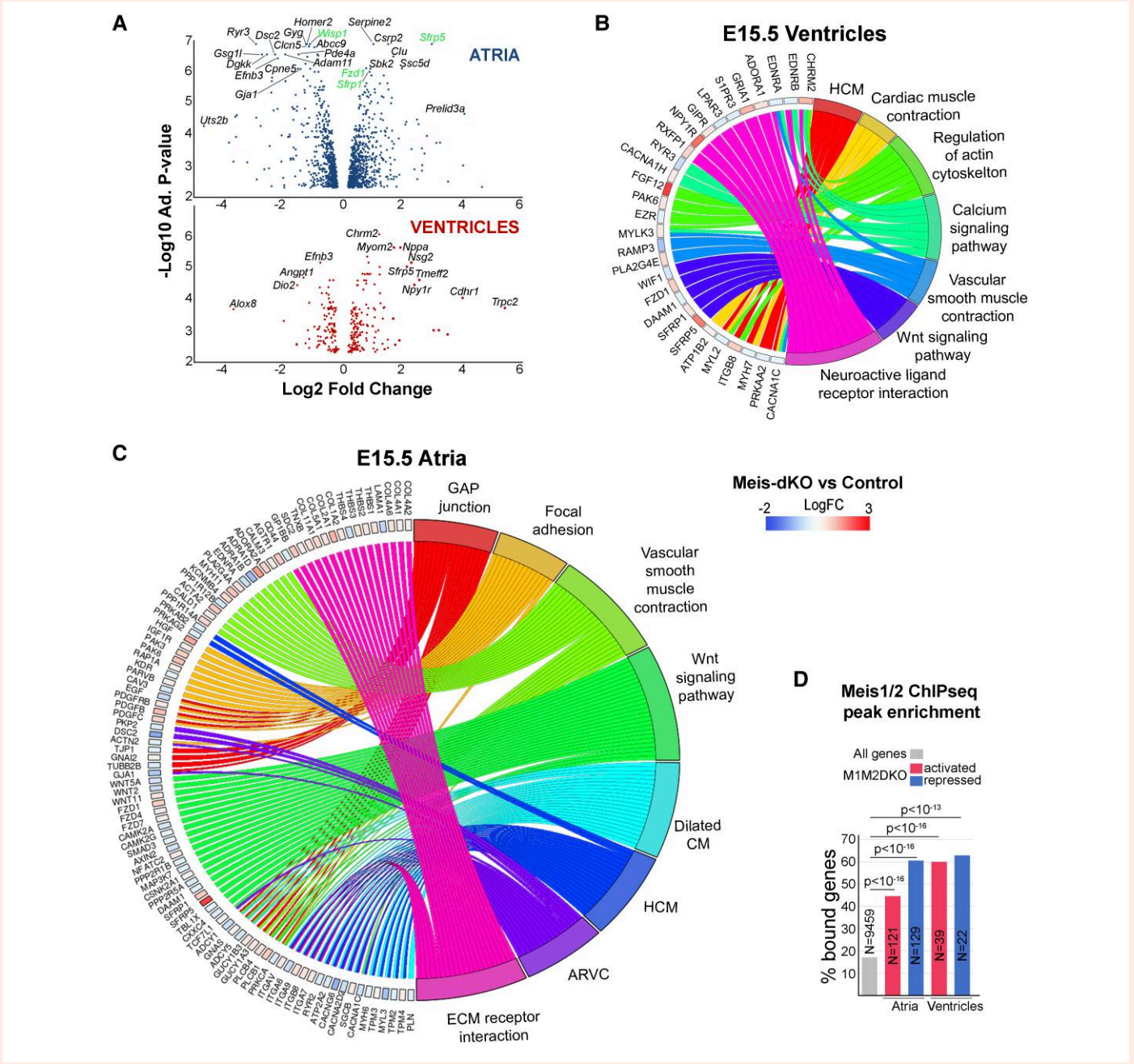

Figure 3 Transcriptomic analysis of mutant hearts with cardiomyocyte-specific *Meis1* and *Meis2* deletion. (*A*) Volcano plots showing transcriptome changes in atria (above) and ventricles (below) of E15.5 M1M2DKO hearts. $n = 4$ control and 4 mutant specimens. Some genes potentially relevant in cardiac biology are highlighted. For the analysis in atria, genes of the Gene Ontology class 'Wnt signalling pathway' are shown. (*B* and *C*) Gene ontology plots summarizing results from gene set enrichment analysis in E15.5 M1M2DKO ventricles (*B*) and atria (*C*). Genes and fold changes are represented on the left side and the associated disease categories on the right side. (*D*) Graph showing the over-representation of genes bound by Meis1/2 (ChIP-seq peaks from 3 kb upstream to1 kb downstream; data from[36]) within the genes activated (≥1.5-fold) or repressed (≤−1.5-fold) in the RNA-seq analysis in E15.5 atria and ventricles. χ^2 test with two-tailed *P*-values.

and those genes that have nearby Meis1/2-binding sites in the heart[36] (*Figure 3D*; see Supplementary material online, *Dataset S3*). These results show that the RNA-seq analysis identifies direct Meis targets.

3.3 Association of *Meis1* and *Meis2* functions with CCS development and foetal function

These previous observations, together with the preferential expressions of *Meis1* and *Meis2* in various components of the adult CCS, led us to specifically address the role of Meis TFs in cardiac conduction. We therefore studied the correlation between Meis-regulated genes and a list of genes functionally associated with progressive CCS disease in humans[43] and found a strong association (*Figure 4A*). In addition, other studies identified Meis-binding sites enriched in open chromatin regions in mouse SAN cardiomyocytes[37] and in human pacemaker-like cardiomyocytes derived from induced pluripotent stem cells (IPSCs).[45] We then mapped the co-occurrence of ATAC-seq peaks in right atrium (RA) and pacemaker cardiomyocytes from[37] and Meis ChIP-seq-binding sites from[36] and associated

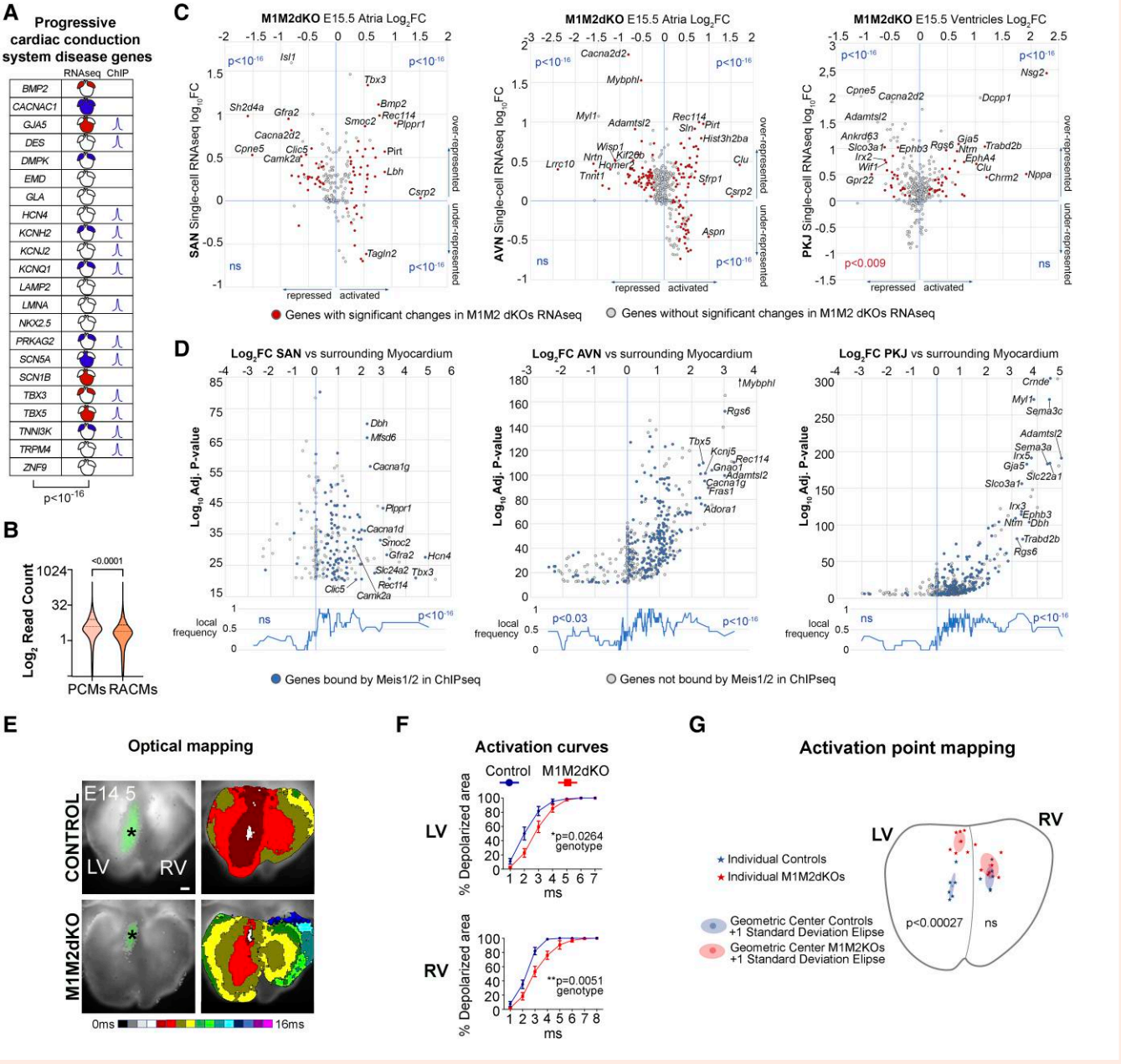

Figure 4 Elimination of Meis function affects the CCS during heart development. (*A*) Graphic table shows the incidence of Meis regulation and binding to genes associated to progressive cardiac conduction disease. Blue filling indicates repression in M1M2DKO and red filling activation in M1M2DKO of the indicated gene in the coloured heart region. The presence of a Meis1/2 ChIP-seq peak[36] from 3 kb upstream to 1 kb downstream of the transcription unit is represented by a ChIP-seq 'peak' icon. χ^2 test with Yate's correction and two-tailed *P*-values. (*B*) Violin plot representing the distribution of reads/peak in ATAC-seq peaks[37] coincident with Meis ChIP-seq-binding sites[36] in RA CMs and pacemaker CMs. The dotted lines show the median and quartiles. Wilcoxon matched-pairs signed rank test. Two-tailed *P*-value <0.0001. (*C*) Plots correlating single-cell RNA-seq fold-change between CCS cardiomyocytes and nearby non-CCS cardiomyocytes from,[44] with RNA-seq fold-change upon Meis1/2 elimination in cardiomyocytes. $n = 4$ control and 4 mutant specimens for RNA-seq of Meis mutants. Dots highlighted in red indicate genes that change significantly in the Meis1/2 mutant hearts. From left to right, graphs show the comparison of Meis1/2 mutant atria with the SAN region, Meis1/2 mutant atria with the AVN region, and Meis1/2 mutant ventricles with the VCS region. (*D*) Volcano plots showing the distribution of single-cell RNA-seq fold-change between CCS cardiomyocytes and nearby non-CCS cardiomyocytes from[44] with highlight of the genes bound by Meis1/2 in ChIP-seq adult heart experiments from.[36] Line graphs below indicate the local enrichment in Meis-bound genes according to the fold enrichment in the single-cell RNA-seq analyses. Data are shown from left to right for the SAN, AVN, and VCS regions. χ^2 test with Yate's correction and two-sided *P*-values. (*E*) Representative optical maps of ventricular depolarization (dorsal side) in control and M1M2DKO hearts at E14.5. *The area where the first signal appears. Colour bar shows the temporal scale (each colour = 1 ms). Scale bar: 200 µm. (*F*) LV and RV activation curves showing depolarized area percentage per millisecond obtained from the maps ($n = 8$/group). Graphs show the mean ± SEM. Two-way ANOVA with Sidak's correction for multiple measurements and two-sided *P*-value. (*G*) Map of the ventricular conduction activation points (or breakthrough point), indicated with an asterisk for each control and mutant hearts, including representation of the geometric centre and a standard deviation ellipse (dorsal view). $n = 6$ control and 7 mutant specimens. Type II multivariate analysis of variance (MANOVA) test with Pillai statistics was applied to the orthogonal co-ordinates defining the position of each activation point.

them to specific genes by mapping their presence within −1 to +1 kb from the transcription units. We then identified the overlap between these genes and those that change expression in M1M2DKO mutants (see Supplementary material online, *Dataset S4*). This study showed that of the 1282 genes affected by Meis mutation in atria, 32% contained a Meis peak coincident with an ATAC-seq peak in RA CMs (see Supplementary material online, *Dataset S4*). This proportion was 35% for genes with Meis and ATAC-seq peaks in pacemaker CMs. The identified genes represent good candidates for direct Meis targets in atrial and SAN CMs. There was a strong overlap between these candidate Meis targets in atrial and pacemaker CMs, with very few genes specific for atria, but a group of 50 genes specific for pacemaker CMs (see Supplementary material online, *Dataset S4*). Although the proportion of genes with ATAC-seq + Meis peaks was only slightly higher in pacemaker CMs than in RA CMs, the opening of the ATAC-seq peaks coincident with Meis peaks was on average higher in pacemaker CMs than in RA CMs, as measured by the number of reads in each peak (*Figure 4B*; see Supplementary material online, *Dataset S5*). The presence of ATAC-seq + Meis peaks was about double as frequent within the group of genes down-regulated in mouse mutants than in the up-regulated ones. This suggests that Meis is predominantly an activator rather than a repressor on direct targets in CMs. These results indicate Meis roles and target genes in both atrial and pacemaker CMs.

To more specifically study the correlation between genes regulated by Meis TF and the transcriptional signature of the CCS, we compared a published single-cell RNA-seq analysis of the different components of the E16 CCS[44] with the set of genes de-regulated in E15.5 M1M2DKO hearts. We found a very strong association between the genes down-regulated in M1M2DKO (genes activated by Meis) and those found in the single-cell analysis to have preferential expression in the SAN, the AVN, and the Purkinje (PKJ) cardiomyocytes (*Figure 4C*, left superior quadrant of each graph; see Supplementary material online, *Datasets S6–S8*). In contrast, genes down-regulated in M1M2DKO are not found among those whose expression level in SAN, AVN, or PKJ cardiomyocytes is similar or lower to that to surrounding non-CCS cardiomyocytes (*Figure 4C*, left inferior quadrant of each graph + genes grouping around 0 in the vertical axis; see Supplementary material online, *Datasets S6–S8*). In contrast, genes up-regulated in M1M2DKO (genes repressed by Meis) were found in both, the set of genes with higher expression in the SAN and AVN cardiomyocytes and the set of genes with lower expression in the SAN and AVN cardiomyocytes compared with surrounding non-CCS cardiomyocytes (*Figure 4C*, right upper and lower quadrants of each graph; see Supplementary material online, *Datasets S6* and *S7*). In the case of PKJ cardiomyocytes, genes up-regulated in M1M2KO only showed clear association with genes preferentially expressed in PKJ cardiomyocytes (*Figure 4C*, right upper quadrant; see Supplementary material online, *Dataset S8*). A study of the distribution of Meis ChIP-seq peaks[36] showed that only genes with higher expression in SAN, AVN, or PKJ cardiomyocytes than in non-CCS cardiomyocytes strongly associate with Meis-bound genes (*Figure 4D*). To determine whether some of these findings correlate with expression changes at the level of protein expression, we characterized by immunocytochemistry the expression of SH2D4a, an adapter protein that regulates several signalling pathways,[46–48] is preferentially expressed in the SAN (*Figure 4C* and the study by Goodyer *et al.*[44]) and shows lower expression in M1M2DKO atria by RNA-seq (*Figure 4C*). We found widespread low expression of SH2D4a in cardiomyocytes of control mice, with the exception of the SAN, in which a strong expression was found (see Supplementary material online, *Figure S2*). In M1M2DKO mutants, SH2D4a expression was strongly reduced in general and specifically in the SAN, where the strong expression was lost (see Supplementary material online, *Figure S2*). We also tested the expression of the EPHB3 protein, a receptor involved in cell–cell communication that is preferentially expressed in the ventricular conduction system (VCS) (*Figure 4C* and the studies by Goodyer *et al.*[44] and van Eif *et al.*[49]) and shows reduced expression in M1M2DKO mutants by RNA-seq (*Figure 4C*). In control hearts, we found expression of EPHB3 in the AVB, BB, and sub-endothelial cardiomyocytes (see Supplementary material online, *Figure S2*), the latter being coincident with the location of the PKJ fibres. In M1M2DKO mutants, we could not detect any EPHB3 expression (see Supplementary material online, *Figure S2*). Together, these findings show that Meis controls the gene regulatory network typical of cardiomyocytes in various components of the CCS, with predominance of activating interactions, but also performing some repressive activities.

Next, we studied whether these changes in gene expression translate into functional alterations of cardiac conduction. For this, we first studied foetal cardiac conduction at E14.5 using an optical mapping approach to record epicardial voltage activation maps (*Figure 4E*). We found prolonged activation time in both, the right and the LVs (*Figure 4E* and *F*). No alterations were found in atrial conduction velocity in these analyses (not shown). The functional maturation of the His-PKJ system can be monitored during development by the progressive displacement of the breakthrough activation point from the base to the apex of the ventricles.[50,51] We therefore mapped the breakthrough point and found that in the LV it was more basally located in mutants compared with controls, while in the RV a non-significant but similar tendency was observed (*Figure 4G*). These observations indicate delayed maturation of the VCS, in agreement with the alterations found in gene expression.

3.4 *Meis1* and *Meis2* maintain CCS function during adult life

The previous results suggest a predominant role of Meis TFs in the development and adult physiology of components of the CCS; however, the M1M2DKO model does not sort out functions in working vs. CCS cardiomyocytes and does not allow functional analyses in the adult heart. To overcome this limitation, we generated a model in which we used *Hcn4*^{CreERT2} [28] to specifically recombine the floxed Meis alleles in the CCS of adult mice (M1M2 CSiKO, *Figure 5A–C*). We administered tamoxifen at 2 months of age and then followed the time course of several ECG parameters (*Figure 5D–K*; see Supplementary material online, *Figure S3*) up to 24 months. As expected, the tamoxifen treatment led to elimination of Meis expression in components of the CCS without obvious anatomical alterations (see Supplementary material online, *Figure S4*). The analysis of the ECG showed an early (starting 1 month after tamoxifen administration) and statistically significant prolongation of the PR interval in mutants (*Figure 5D*). Time course comparisons using a mixed model analysis of variance (ANOVA) also showed higher amplitude values of the P-wave in the M1M2 CSiKO mice compared with controls (*Figure 5E*), without significant changes in P-wave duration between groups (*Figure 5F*). The prolongation of the PR interval suggests an underlying impairment of atrio-ventricular conduction in M1M2 CSiKO. In contrast, all analyses involving the QRS complex (QRS duration and amplitude) were not statistically different between mutants and controls (*Figure 5G* and *H*). The latter suggests no impairment in the VCS. Overall, heart rate values assessed using RR intervals were not statistically different between groups (*Figure 5I*). However, further analysis using RR interval variability to address SAN function (in the absence of atrial or ventricular premature complexes) identified overt differences in RR interval variability between groups (*Figure 5J* and *K*). The latter was compatible with higher prevalence of sinus node dysfunction in mutants compared with controls. Such rhythm alterations were characterized by rapid oscillations in R–R intervals due to irregular P-waves (with sinus node morphology) in singular or periodic episodes (*Figure 5L*; see Supplementary material online, *Figure S3*). Moreover, further analysis of the time course incidence of such alterations in RR interval variability showed early onset in M1M2CSiKO mice (already detected at 2 and 6 months after tamoxifen treatment in 5 of 17 animals) compared with controls, in which only one animal showed abnormal RR interval variability at 24 months of age (*Figure 5M*; see Supplementary material online, *Figure S3*). In all animals, once sinus node dysfunction was detected, the alteration was present during the follow-up if the animal was still alive.

The elongation of the PR interval in M1M2 CSiKO mice evokes the human GWAS analyses in which *Meis1* single-nucleotide polymorphisms (SNPs) located in Intron 8 associate with PR interval elongation[20,21] (*Figure 6A*). Interestingly, SNP variants in Intron 8 associate as well with the restless

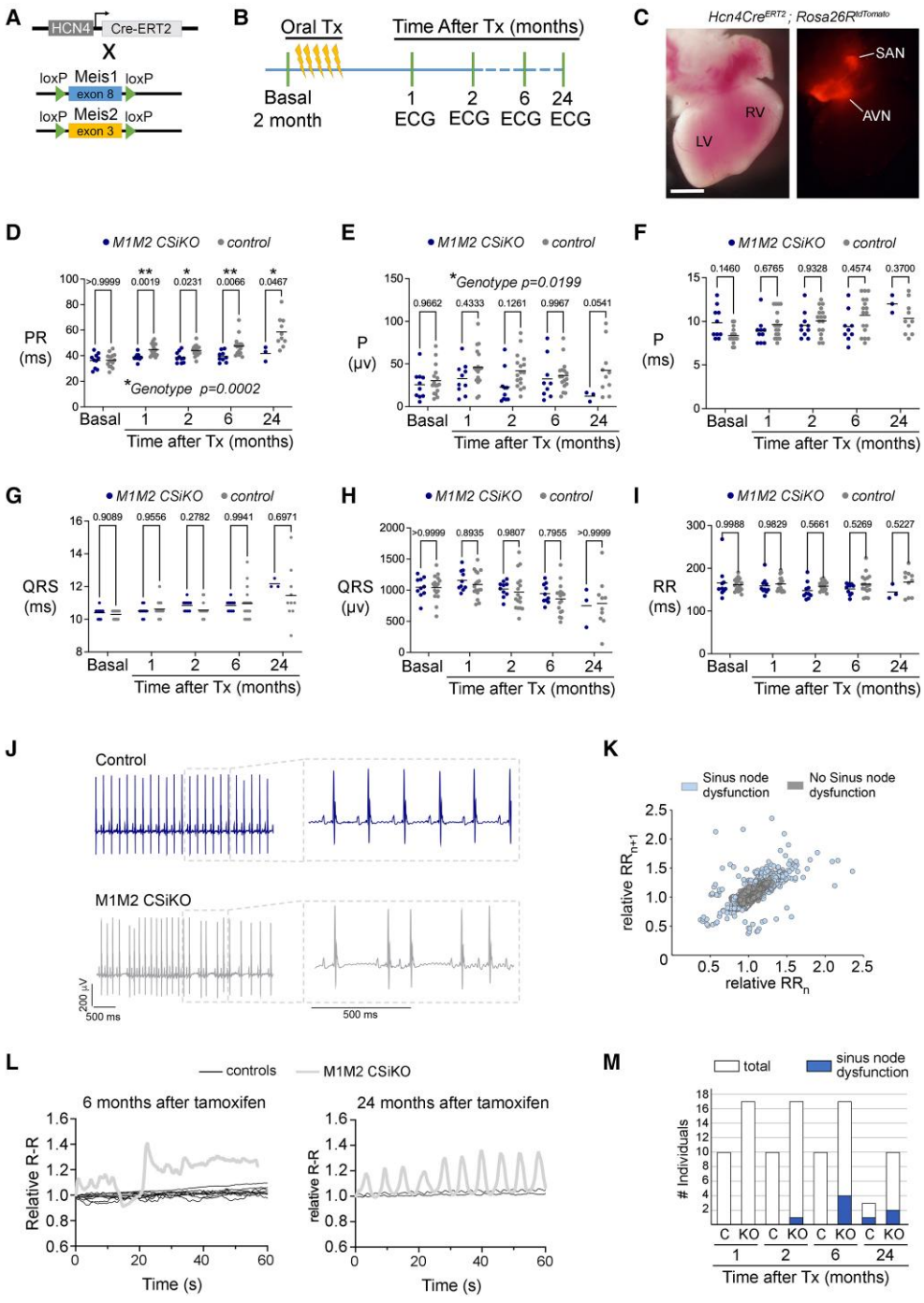

Figure 5 Conditional elimination of Meis function in the adult CCS produces progressive dysfunction of sinus rhythm function and PR elongation. (*A*) Model for double deletion of *Meis1* and *Meis2* in the conduction system using *Hcn4*^{CreERT2}. (*B*) Experimental timeline showing tamoxifen treatment and the schedule for the electrocardiographic analyses. (*C*) Dorsal views in brightfield and epifluorescence of a tamoxifen-induced newborn heart in which Tomato reports the sites of Cre activity provided by the *Hcn4*^{CreERT2} allele. Scale bar: 1 mm. (*D–I*) Representation of the values for different parameters of the ECG analyses in control and mutant M1M2 CSiKO mice before tamoxifen administration (basal) and at different times after tamoxifen administration. Each dot represents the average value for a single specimen. $n = 10$ control and 16 mutant in basal, 10 control and 16 mutant at 1 and 2 months, 9 control and 17 mutant at 6 months, and 3 control and 10 mutant at 24 months. Mixed model ANOVA with Sidak's correction for multiple measurements and two-tailed *P*-values. Adjusted *P*-values are shown for each individual comparison. The *P*-value for the global analysis of the 'genotype' variable is shown only in case of significance. (*J*) Examples of ECGs of control and M1M2 CSiKO showing sinus rhythm dysfunction. (*K*) Poincaré plot of the RRn to RRn + 1 correlation in relative terms for all analysed data in (*D–I*) (right). The domain for 'no sinus node dysfunction' was determined from control animals of up to 6 months of age, whereas all points outside this domain correspond to mutants up to 6 months of age. (*L*) Example of sinus rhythm alteration in the same mutant specimen 6 months and 2 years after tamoxifen administration. (*M*) Bar plot showing the incidence of sinus node dysfunction in control and mutant M1M2 CSiKO mice at different times after tamoxifen administration for all analysed data in (*D–I*).

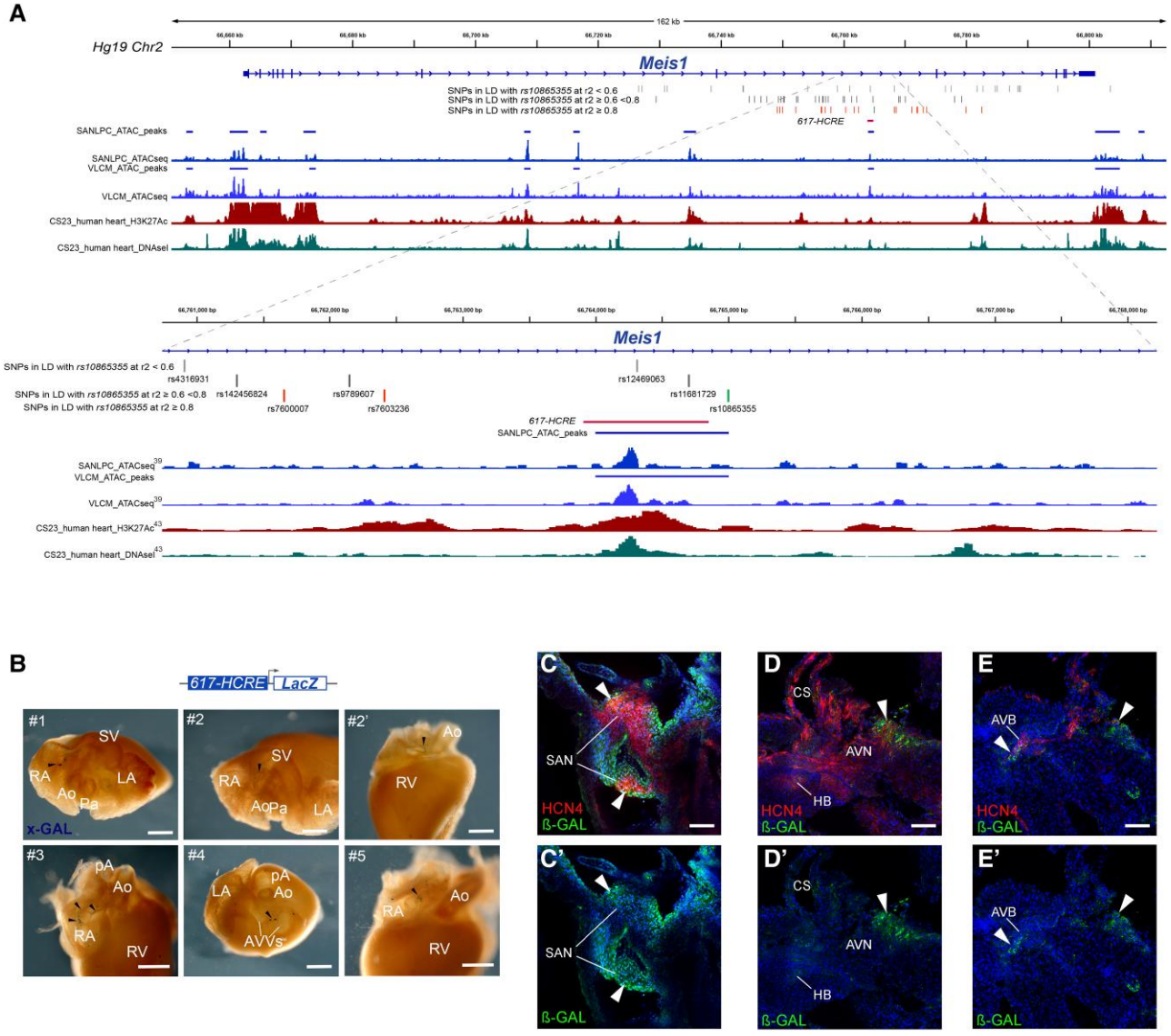

Figure 6 A Meis1 human enhancer in a GWAS-identified intron associated with PR elongation drives expression in CCS cardiomyocytes. (*A*) The Meis1 genomic region showing SNPs in different degrees of LD with the lead SNP associated with PR elongation (rs10865355). SNP linkage data were retrieved from LD information from the European ancestry (EUR) dataset of the 1000 Genomes Phase 3 project for rs10865355 using the LDproxy Tool provided by LDLink (https://ldlink.nci.nih.gov/?tab=ldproxy). The full list of SNPs is provided in Supplementary material online, *Dataset S9*. Below, a zoom-in to Intron 8, where the PR elongation–associated SNPs are located. Potential regulatory elements are indicated by epigenetic marks and detection of open chromatin by ATAC-seq in pacemaker-like CMs and ventricular-like CMs derived from human IPSCs (hIPSCs) and the developing human heart. The location of the *617-HCRE* enhancer, previously characterized in the context of the RLS syndrome,[29] is also shown. (*B*) Scheme showing the transgene carrying *LacZ* gene under the control of *617-HCRE* and brightfield images of five different E17.5 transgenic hearts stained for LacZ. Arrowheads indicate the areas of LacZ expression. Scale bars: 500 µm. (*C–E*) Confocal images of co-immunofluorescence of β-galactosidase and Hcn4 in sections from transgenic hearts at E17.5. Arrowheads indicate the areas of co-expression at the SAN, AVN, and AVB. (*C'–E'*) Single channel images from (*C–E*) with β-galactosidase expression. Ao, aorta; Pa, pulmonary artery; SV, sinus venosus; AVVs, atrio-ventricular valves.

legs syndrome (RLS) in humans[52] (*Figure 6A*), and a highly conserved regulatory element (*617-HCRE*) of the human *Meis1* Intron 8 shows enhancer activity related to RLS[29] (*Figure 6A*). This regulatory element is nearby the lead SNP associated with PR interval elongation (rs10865355); however, no functional SNP has been related yet to PR elongation in this region. Examination of previously described functional genomics datasets[45,53] shows that the only genomic segment with cardiac enhancer marks in the genomic region that contains SNPs in high linkage disequilibrium (LD) with rs10865355 is coincident with *617-HCRE* (*Figure 6A*). We thus studied the cardiac expression of a mouse transgene with the *LacZ* reporter under the control of the *617-HCRE* enhancer (*Figure 6B*). We found cardiac expression of the reporter in six of nine specimens. Expression was detected in small cell patches, which suggests variable mosaic expression of the transgene. In all six specimens, we found patches of cells potentially affecting the atrial and atrio-ventricular conduction system, including the SAN (*Figure 6B*, Specimens #1, #2, and #5), the inter-nodal tracks (*Figure 6B*, Specimen #3), and the AVN (*Figure 6B*, Specimen #4). Co-detection of β-galactosidase with Hcn4 in sections confirmed the expression of the transgene in cardiomyocytes of

the SAN, AVN, AVB, and adjacent regions (*Figure 6C–E'*). These results demonstrate that the *617-HCRE* activity contributes to *Meis1* expression in various components of the CCS, providing a potential mechanistic basis for the observed *Meis1*-linked PR elongation in humans.

4. Discussion

Although *Meis2* is involved in human congenital malformations[17–19] and *Meis1* has been associated to PR elongation in humans[20,21] and to regenerative ability in mice,[16] a systematic analysis of *Meis1* and *Meis2* functions during the cardiomyocyte life cycle had not been performed. Given the strong similarity between Meis1 and Meis2 proteins and their frequent co-expression, we decided to perform a combined deletion of both genes in cardiomyocytes. A third gene encoding a TF of the family, *Meis3*, is expressed at low levels in cardiomyocytes[54] and does not get activated in *Meis1/2* mutants (see RNA-seq results). Therefore, the models reported here largely eliminate Meis function in cardiomyocytes. A detailed expression analysis revealed the preferential expressions of Meis1 and Meis2 in the SAN, AVN, and AVB cardiomyocytes, and deletion of Meis genes showed alterations in cardiac conduction, both during development and in adult life. Interestingly, the observations in adult mice correlate well with the association of *Meis1* with PR elongation by GWAS in humans. Furthermore, we found that a mechanistic basis can be proposed between the activity of human *Meis1* enhancer *617-HCRE* and Meis function in cardiac conduction. In addition, we found alterations on sinus node function and impulse propagation in the deletion of *Meis1* and *Meis2* from the adult CCS. These results suggest a wide involvement of Meis activity in regulating different components of the CCS, not only during development but also, more intriguingly, during the maintenance of SAN pacemaker activity and atrio-ventricular conduction in adulthood. These observations suggest that not only congenital Meis mutations but also alterations of Meis expression during adult life in cardiomyocytes of the SAN and atrio-ventricular conduction system may lead to progressive CCS disease. Interestingly, previous studies during limb induction have shown functional co-operation between Meis factors and Tbx5 through binding to common DNA sites,[5] while Tbx5 is required for VCS development and adult function maintenance.[55] Similarly, Shox2, which is needed for SAN development, is also important for limb proximal-to-distal patterning, and Meis TFs are upstream regulators of *Shox2* transcription during limb development.[5] In addition, Nkx2.5 needs to be repressed from the prospective sinus node head for its proper specification,[56] and Meis1 has been shown to antagonize Nkx2.5 on DNA-binding sites during anterior second heart field (SHF) differentiation.[57] These correlations suggest that transcriptional regulatory modules involving Meis and other TFs co-opted during patterning of different organs.

In addition, VSD and atrial malformations were observed following Meis genes deletion during gestation, indicating functions beyond the development and function of the CCS. Although these morphological alterations could be envisioned as the cause of perinatal death of the mutants, functional analyses of fetuses at term do not detect heart failure, which suggests that perinatal electrical failure may underlie the observed lethality. The morphological alterations in atria are striking and suggest strong alteration of atrial patterning mechanisms. One of the pathways strongly altered in fetal hearts was the Wnt pathway, and the factors involved preferentially contained those related to the planar cell polarity (PCP) pathway,[58] including ligands Wnt5a and Wnt11 and receptors Fzd1, 4, and 7. Since the PCP pathway is generally involved in morphogenesis, it is likely involved in the morphological alterations found in the atria. Furthermore, deletion of Wnt5a,[59] Wnt11,[60] and Fzd1[61] and Fdz7[62] leads to OFT defects including VSD, double outlet right ventricle (DORV), persistent truncus arteriosus, and transposition of the great arteries, which suggests that the alterations of OFT patterning in Meis mutants are also related to failure in proper regulation of the PCP pathway.

Our study identifies multiple roles of Meis TFs during cardiomyocyte development and adult life and shows that they play a predominant role in the development and adult physiology of the SAN and atrio-ventricular conduction, providing models to explain the association between *Meis1* and cardiac conduction alterations in humans.

Supplementary material

Supplementary material is available at *Cardiovascular Research* online.

Authors' contributions

N.M.-M.: conceptualization, experimentation, methodology, data analysis, manuscript writing, and manuscript correction. A.S.-C.: data analysis and manuscript correction. C.D.-D.: immunofluorescence analyses. S.T.: methodology. V.C.: methodology. I.E.: methodology. A.L.: provision of transgenic mouse line. B.S.: GWAS and LD data curation. J.W.: provision of transgenic mouse line, GWAS and LD data curation, and manuscript correction. V.O.: experimentation and methodology. D.S.: conceptualization, experimentation, methodology, data analysis, and manuscript correction. D.F.-R.: conceptualization, data analysis, and manuscript correction. M.T.: conceptualization, experimentation, methodology, data analysis, manuscript writing, and manuscript correction.

Acknowledgements

We thank members of the Torres laboratory for fruitful discussions and advice on this work, Fátima Sánchez-Cabo for helpful advice on the statistics, and Morena Raiola for help in figure design. We thank the CNIC Technical Units for Compared Medicine, Advanced Imaging, Bioinformatics and Genomics.

Conflict of interest: none declared.

Funding

This work was supported by the H2020 Societal Changes Program (grant number SC1-BHC-07-2019. Ref. 874764 'REANIMA' to M.T.); the Spanish Ministerio de Ciencia e Innovación (grant numbers PGC2018-096486-B-I00 and PID2022-140058NB-C31 to M.T. and PID2019-109329RB-I00 to D.F.-R.); the Comunidad de Madrid (P2022/BMD-7245 CARDIOBOOST-CM to M.T.); the Ministry of Education, Youth and Sports of the Czech Republic (grant number co-operation 207029 cardiovascular science to D.S.); the Czech Science Foundation (grant numbers 18-03461S and 22-05271S to D.S.); 'la Caixa' Foundation Severo Ochoa PhD Fellowship (grant numbers 100010434 to N.M.-M. and LCF/BQ/DR19/11740029 to A.S.-C.); European Molecular Biology Organization (EMBO) short-term fellowship (grant number 7667 to N.M.-M.). The CNIC is supported by the Ministerio de Ciencia e Innovación and the Pro CNIC Foundation and is a Severo Ochoa Center of Excellence (grant number CEX2020-001041-S, funded by MICIU/AEI/10.13039/501100011033).

Data availability

The data underlying this article are available in the article and in its online supplementary material.

References

1. Longobardi E, Penkov D, Mateos D, De Florian G, Torres M, Blasi F. Biochemistry of the tale transcription factors PREP, MEIS, and PBX in vertebrates. *Dev Dyn* 2014;**243**:59–75.
2. Moscow JA, Huang H, Carter C, Hines K, Zujewski J, Cusack G, Chow C, Venzon D, Sorrentino B, Chiang Y, Goldspiel B, Leitman S, Read EJ, Abati A, Gottesman MM, Pastan I, Sellers S, Dunbar C, Cowan KH. Engraftment of MDR1 and NeoR gene-transduced hematopoietic cells after breast cancer chemotherapy. *Blood* 1999;**94**:52–61.
3. Oulad-Abdelghani M, Chazaud C, Bouillet P, Sapin V, Chambon P, Dollé P. Meis2, a novel mouse Pbx-related homeobox gene induced by retinoic acid during differentiation of P19 embryonal carcinoma cells. *Dev Dyn* 1997;**210**:173–183.
4. Nakamura T, Jenkins NA, Copeland NG. Identification of a new family of Pbx-related homeobox genes. *Oncogene* 1996;**13**:2235–2242.
5. Delgado I, Giovinazzo G, Temiño S, Gauthier Y, Balsalobre A, Drouin J, Torres M. Control of mouse limb initiation and antero-posterior patterning by Meis transcription factors. *Nat Commun* 2021;**12**:3086.

6. Mann RS, Affolter M. Hox proteins meet more partners. *Curr Opin Genet Dev* 1998;**8**: 423–429.
7. Azcoitia V, Aracil M, Martinez-A C, Torres M. The homeodomain protein Meis1 is essential for definitive hematopoiesis and vascular patterning in the mouse embryo. *Dev Biol* 2005; **280**:307–320.
8. Carramolino L, Fuentes J, García-Andrés C, Azcoitia V, Riethmacher D, Torres M. Platelets play an essential role in separating the blood and lymphatic vasculatures during embryonic angiogenesis. *Circ Res* 2010;**106**:1197–1201.
9. Hisa T, Spence SE, Rachel RA, Fujita M, Nakamura T, Ward JM, Devor-Henneman DE, Saiki Y, Kutsuna H, Tessarollo L, Jenkins NA, Copeland NG. Hematopoietic, angiogenic and eye defects in Meis1 mutant animals. *EMBO J* 2004;**23**:450–459.
10. Stankunas K, Shang C, Twu KY, Kao SC, Jenkins NA, Copeland NG, Sanyal M, Selleri L, Cleary ML, Chang CP. Pbx/Meis deficiencies demonstrate multigenetic origins of congenital heart disease. *Circ Res* 2008;**103**:702–709.
11. Gonzalez-Lazaro M, Rosello-Diez A, Delgado I, Carramolino L, Angeles Sanguino M, Giovinazzo G, Torres M. Two new targeted alleles for the comprehensive analysis of Meis1 functions in the mouse. *Genesis* 2014;**52**:967–975.
12. Machon O, Masek J, Machonova O, Krauss S, Kozmik Z. Meis2 is essential for cranial and cardiac neural crest development. *BMC Dev Biol* 2015;**15**:40.
13. Unnisa Z, Clark JP, Roychoudhury J, Thomas E, Tessarollo L, Copeland NG, Jenkins NA, Grimes HL, Kumar AR. Meis1 preserves hematopoietic stem cells in mice by limiting oxidative stress. *Blood* 2012;**120**:4973–4981.
14. Simsek T, Kocabas F, Zheng J, Deberardinis RJ, Mahmoud AI, Olson EN, Schneider JW, Zhang CC, Sadek HA. The distinct metabolic profile of hematopoietic stem cells reflects their location in a hypoxic niche. *Cell Stem Cell* 2010;**7**:380–390.
15. Kocabas F, Zheng J, Thet S, Copeland NG, Jenkins NA, DeBerardinis RJ, Zhang C, Sadek HA. Meis1 regulates the metabolic phenotype and oxidant defense of hematopoietic stem cells. *Blood* 2012;**120**:4963–4972.
16. Mahmoud AI, Kocabas F, Muralidhar SA, Kimura W, Koura AS, Thet S, Porrello ER, Sadek HA. Meis1 regulates postnatal cardiomyocyte cell cycle arrest. *Nature* 2013;**497**:249–253.
17. Louw JJ, Corveleyn A, Jia Y, Hens G, Gewillig M, Devriendt K. MEIS2 involvement in cardiac development, cleft palate, and intellectual disability. *Am J Med Genet A* 2015;**167**:1142–1146.
18. Verheije R, Kupchik GS, Isidor B, Kroes HY, Lynch SA, Hawkes L, Hempel M, Gelb BD, Ghoumid J, D'Amours G, Chandler K, Dubourg C, Loddo S, Tumer Z, Shaw-Smith C, Nizon M, Shevell M, Van Hoof E, Anyane-Yeboa K, Cerbone G, Clayton-Smith J, Cogne B, Corre P, Corveleyn A, De Borre M, Hjortshoj TD, Fradin M, Gewillig M, Goldmuntz E, Hens G, Lemyre E, Journel H, Kini U, Kortum F, Le Caignec C, Novelli A, Odent S, Petit F, Revah-Politi A, Stong N, Strom TM, van Binsbergen E, DDD study; Devriendt K, Breckpot J. Heterozygous loss-of-function variants of MEIS2 cause a triad of palatal defects, congenital heart defects, and intellectual disability. *Eur J Hum Genet* 2019;**27**:278–290.
19. Giliberti A, Currò A, Papa FT, Frullanti E, Ariani F, Coriolani G, Grosso S, Renieri A, Mari F. MEIS2 gene is responsible for intellectual disability, cardiac defects and a distinct facial phenotype. *Eur J Med Genet* 2020;**63**:103627.
20. Pfeufer A, van Noord C, Marciante KD, Arking DE, Larson MG, Smith AV, Tarasov KV, Muller M, Sotoodehnia N, Sinner MF, Verwoert GC, Li M, Kao WH, Kottgen A, Coresh J, Bis JC, Psaty BM, Rice K, Rotter JI, Rivadeneira F, Hofman A, Kors JA, Stricker BH, Uitterlinden AG, van Duijn CM, Beckmann BM, Sauter W, Gieger C, Lubitz SA, Newton-Cheh C, Wang TJ, Magnani JW, Schnabel RB, Chung MK, Barnard J, Smith JD, Van Wagoner DR, Vasan RS, Aspelund T, Eiriksdottir G, Harris TB, Launer LJ, Najjar SS, Lakatta E, Schlessinger D, Uda M, Abecasis GR, Muller-Myhsok B, Ehret GB, Boerwinkle E, Chakravarti A, Soliman EZ, Lunetta KL, Perz S, Wichmann HE, Meitinger T, Levy D, Gudnason V, Ellinor PT, Sanna S, Kaab S, Witteman JC, Alonso A, Benjamin EJ, Heckbert SR. Genome-wide association study of PR interval. *Nat Genet* 2010;**42**:153–159.
21. Smith JG, Magnani JW, Palmer C, Meng YA, Soliman EZ, Musani SK, Kerr KF, Schnabel RB, Lubitz SA, Sotoodehnia N, Redline S, Pfeufer A, Müller M, Evans DS, Nalls MA, Liu Y, Newman AB, Zonderman AB, Evans MK, Deo R, Ellinor PT, Paltoo DN, Newton-Cheh C, Benjamin EJ, Mehra R, Alonso A, Heckbert SR, Fox ER; Candidate-gene Association Resource (CARe) Consortium. Genome-wide association studies of the PR interval in African Americans. *PLoS Genet* 2011;**7**:e1001304.
22. van Eif VWW, Devalla HD, Boink GJJ, Christoffels VM. Transcriptional regulation of the cardiac conduction system. *Nat Rev Cardiol* 2018;**15**:617–630.
23. Frank DU, Carter KL, Thomas KR, Burr RM, Bakker ML, Coetzee WA, Tristani-Firouzi M, Bamshad MJ, Christoffels VM, Moon AM. Lethal arrhythmias in Tbx3-deficient mice reveal extreme dosage sensitivity of cardiac conduction system function and homeostasis. *Proc Natl Acad Sci U S A* 2012;**109**:E154–E163.
24. Takeda M, Briggs LE, Wakimoto H, Marks MH, Warren SA, Lu JT, Weinberg EO, Robertson KD, Chien KR, Kasahara H. Slow progressive conduction and contraction defects in loss of Nkx2-5 mice after cardiomyocyte terminal differentiation. *Lab Invest* 2009;**89**:983–993.
25. Madisen L, Zwingman TA, Sunkin SM, Oh SW, Zariwala HA, Gu H, Ng LL, Palmiter RD, Hawrylycz MJ, Jones AR, Lein ES, Zeng H. A robust and high-throughput Cre reporting and characterization system for the whole mouse brain. *Nat Neurosci* 2010;**13**:133–140.
26. Delgado I, López-Delgado AC, Roselló-Díez A, Giovinazzo G, Cadenas V, Fernández-de-Manuel L, Sánchez-Cabo F, Anderson MJ, Lewandoski M, Torres M. Proximo-distal positional information encoded by an Fgf-regulated gradient of homeodomain transcription factors in the vertebrate limb. *Sci Adv* 2020;**6**:eaaz0742.
27. Agah R, Frenkel PA, French BA, Michael LH, Overbeek PA, Schneider MD. Gene recombination in postmitotic cells. Targeted expression of Cre recombinase provokes cardiac-restricted, site-specific rearrangement in adult ventricular muscle in vivo. *J Clin Invest* 1997;**100**:169–179.
28. Hoesl E, Stieber J, Herrmann S, Feil S, Tybl E, Hofmann F, Feil R, Ludwig A. Tamoxifen-inducible gene deletion in the cardiac conduction system. *J Mol Cell Cardiol* 2008;**45**:62–69.
29. Spieler D, Kaffe M, Knauf F, Bessa J, Tena JJ, Giesert F, Schormair B, Tilch E, Lee H, Horsch M, Czamara D, Karbalai N, von Toerne C, Waldenberger M, Gieger C, Lichtner P, Claussnitzer M, Naumann R, Muller-Myhsok B, Torres M, Garrett L, Rozman J, Klingenspor M, Gailus-Durner V, Fuchs H, de Angelis MH, Beckers J, Holter SM, Meitinger T, Hauck SM, Laumen H, Wurst W, Casares F, Gomez-Skarmeta JL, Winkelmann J. Restless legs syndrome-associated intronic common variant in Meis1 alters enhancer function in the developing telencephalon. *Genome Res* 2014;**24**:592–603.
30. Mercader N, Tanaka EM, Torres M. Proximodistal identity during vertebrate limb regeneration is regulated by Meis homeodomain proteins. *Development* 2005;**132**:4131–4142.
31. Teichholz LE, Kreulen T, Herman MV, Gorlin R. Problems in echocardiographic volume determinations: echocardiographic-angiographic correlations in the presence of absence of asynergy. *Am J Cardiol* 1976;**37**:7–11.
32. Sankova B, Benes J Jr, Krejci E, Dupays L, Theveniau-Ruissy M, Miquerol L, Sedmera D. The effect of connexin40 deficiency on ventricular conduction system function during development. *Cardiovasc Res* 2012;**95**:469–479.
33. Rivera-Torres J, Calvo CJ, Llach A, Guzman-Martinez G, Caballero R, Gonzalez-Gomez C, Jimenez-Borreguero LJ, Guadix JA, Osorio FG, Lopez-Otin C, Herraiz-Martinez A, Cabello N, Vallmitjana A, Benitez R, Gordon LB, Jalife J, Perez-Pomares JM, Tamargo J, Delpon E, Hove-Madsen L, Filgueiras-Rama D, Andres V. Cardiac electrical defects in progeroid mice and Hutchinson-Gilford progeria syndrome patients with nuclear lamina alterations. *Proc Natl Acad Sci U S A* 2016;**113**:E7250–E7259.
34. Filgueiras-Rama D, Vasilijevic J, Jalife J, Noujaim SF, Alfonso JM, Nicolas-Avila JA, Gutierrez C, Zamarreno N, Hidalgo A, Bernabe A, Cop CP, Ponce-Balbuena D, Guerrero-Serna G, Calle D, Desco M, Ruiz-Cabello J, Nieto A, Falcon A. Human influenza A virus causes myocardial and cardiac-specific conduction system infections associated with early inflammation and premature death. *Cardiovasc Res* 2021;**117**:876–889.
35. Mitchell GF, Jeron A, Koren G. Measurement of heart rate and Q-T interval in the conscious mouse. *Am J Physiol* 1998;**274**:H747–H751.
36. Nguyen NUN, Canseco DC, Xiao F, Nakada Y, Li S, Lam NT, Muralidhar SA, Savla JJ, Hill JA, Le V, Zidan KA, El-Feky HW, Wang Z, Ahmed MS, Hubbi ME, Menendez-Montes I, Moon J, Ali SR, Le V, Villalobos E, Mohamed MS, Elhelaly WM, Thet S, Anene-Nzelu CG, Tan WLW, Foo RS, Meng X, Kanchwala M, Xing C, Roy J, Cyert MS, Rothermel BA, Sadek HA. A calcineurin-Hoxb13 axis regulates growth mode of mammalian cardiomyocytes. *Nature* 2020;**582**:271–276.
37. Galang G, Mandla R, Ruan H, Jung C, Sinha T, Stone NR, Wu RS, Mannion BJ, Allu PKR, Chang K, Rammohan A, Shi MB, Pennacchio LA, Black BL, Vedantham V. ATAC-seq reveals an Isl1 enhancer that regulates sinoatrial node development and function. *Circ Res* 2020;**127**: 1502–1518.
38. Martin M. Cutadapt removes adapter sequences from high-throughput sequencing reads. *EMBnet J* 2011;**17**:10–12.
39. Langmead B, Salzberg SL. Fast gapped-read alignment with Bowtie 2. *Nat Methods* 2012;**9**: 357–359.
40. Zhang Y, Liu T, Meyer CA, Eeckhoute J, Johnson DS, Bernstein BE, Nusbaum C, Myers RM, Brown M, Li W, Liu XS. Model-based analysis of ChIP-Seq (MACS). *Genome Biol* 2008;**9**: R137.
41. Lawrence M, Huber W, Pagès H, Aboyoun P, Carlson M, Gentleman R, Morgan MT, Carey VJ. Software for computing and annotating genomic ranges. *PLoS Comput Biol* 2013;**9**: e1003118.
42. Li H, Handsaker B, Wysoker A, Fennell T, Ruan J, Homer N, Marth G, Abecasis G, Durbin R; 1000 Genome Project Data Processing Subgroup. The sequence alignment/map format and SAMtools. *Bioinformatics* 2009;**25**:2078–2079.
43. Asatryan B, Medeiros-Domingo A. Molecular and genetic insights into progressive cardiac conduction disease. *Europace* 2019;**21**:1145–1158.
44. Goodyer WR, Beyersdorf BM, Paik DT, Tian L, Li G, Buikema JW, Chirikian O, Choi S, Venkatraman S, Adams EL, Tessier-Lavigne M, Wu JC, Wu SM. Transcriptomic profiling of the developing cardiac conduction system at single-cell resolution. *Circ Res* 2019;**125**: 379–397.
45. van Eif VWW, Protze SI, Bosada FM, Yuan X, Sinha T, van Duijvenboden K, Ernault AC, Mohan RA, Wakker V, de Gier-de Vries C, Hooijkaas IB, Wilson MD, Verkerk AO, Bakkers J, Boukens BJ, Black BL, Scott IC, Christoffels VM. Genome-wide analysis identifies an essential human TBX3 pacemaker enhancer. *Circ Res* 2020;**127**:1522–1535.
46. Li T, Li W, Lu J, Liu H, Li Y, Zhao Y. SH2D4A regulates cell proliferation via the ERalpha/PLC-gamma/PKC pathway. *BMB Rep* 2009;**42**:516–522.

47. Ploeger C, Huth T, Sugiyanto RN, Pusch S, Goeppert B, Singer S, Tabti R, Hausser I, Schirmacher P, Desaubry L, Prohibitin RS. STAT3 and SH2D4A physically and functionally interact in tumor cell mitochondria. *Cell Death Dis* 2020;**11**:1023.
48. Yuki R, Ikeda Y, Yasutake R, Saito Y, Nakayama Y. SH2D4A promotes centrosome maturation to support spindle microtubule formation and mitotic progression. *Sci Rep* 2023;**13**: 2067.
49. van Eif VWW, Stefanovic S, Mohan RA, Christoffels VM. Gradual differentiation and confinement of the cardiac conduction system as indicated by marker gene expression. *Biochim Biophys Acta Mol Cell Res* 2020;**1867**:118509.
50. Rentschler S, Vaidya DM, Tamaddon H, Degenhardt K, Sassoon D, Morley GE, Jalife J, Fishman GI. Visualization and functional characterization of the developing murine cardiac conduction system. *Development* 2001;**128**:1785–1792.
51. Gurjarpadhye A, Hewett KW, Justus C, Wen X, Stadt H, Kirby ML, Sedmera D, Gourdie RG. Cardiac neural crest ablation inhibits compaction and electrical function of conduction system bundles. *Am J Physiol Heart Circ Physiol* 2007;**292**:H1291–H1300.
52. Winkelmann J, Schormair B, Lichtner P, Ripke S, Xiong L, Jalilzadeh S, Fulda S, Putz B, Eckstein G, Hauk S, Trenkwalder C, Zimprich A, Stiasny-Kolster K, Oertel W, Bachmann CG, Paulus W, Peglau I, Eisensehr I, Montplaisir J, Turecki G, Rouleau G, Gieger C, Illig T, Wichmann HE, Holsboer F, Muller-Myhsok B, Meitinger T. Genome-wide association study of restless legs syndrome identifies common variants in three genomic regions. *Nat Genet* 2007;**39**: 1000–1006.
53. VanOudenhove J, Yankee TN, Wilderman A, Cotney J. Epigenomic and transcriptomic dynamics during human heart organogenesis. *Circ Res* 2020;**127**:e184–e209.
54. O'Meara CC, Wamstad JA, Gladstone RA, Fomovsky GM, Butty VL, Shrikumar A, Gannon JB, Boyer LA, Lee RT. Transcriptional reversion of cardiac myocyte fate during mammalian cardiac regeneration. *Circ Res* 2015;**116**:804–815.
55. Burnicka-Turek O, Broman MT, Steimle JD, Boukens BJ, Petrenko NB, Ikegami K, Nadadur RD, Qiao Y, Arnolds DE, Yang XH, Patel VV, Nobrega MA, Efimov IR, Moskowitz IP. Transcriptional patterning of the ventricular cardiac conduction system. *Circ Res* 2020; **127**:e94–e106.
56. Li H, Li D, Wang Y, Huang Z, Xu J, Yang T, Wang L, Tang Q, Cai CL, Huang H, Zhang Y, Chen Y. Nkx2-5 defines a subpopulation of pacemaker cells and is essential for the physiological function of the sinoatrial node in mice. *Development* 2019;**146**:dev178145.
57. Dupays L, Shang C, Wilson R, Kotecha S, Wood S, Towers N, Mohun T. Sequential binding of MEIS1 and NKX2-5 on the Popdc2 gene: a mechanism for spatiotemporal regulation of enhancers during cardiogenesis. *Cell Rep* 2015;**13**:183–195.
58. Yang Y, Mlodzik M. Wnt-frizzled/planar cell polarity signaling: cellular orientation by facing the wind (Wnt). *Annu Rev Cell Dev Biol* 2015;**31**:623–646.
59. Schleiffarth JR, Person AD, Martinsen BJ, Sukovich DJ, Neumann A, Baker CV, Lohr JL, Cornfield DN, Ekker SC, Petryk A. Wnt5a is required for cardiac outflow tract septation in mice. *Pediatr Res* 2007;**61**:386–391.
60. Zhou W, Lin L, Majumdar A, Li X, Zhang X, Liu W, Etheridge L, Shi Y, Martin J, Van de VenW, Kaartinen V, Wynshaw-Boris A, McMahon AP, Rosenfeld MG, EvansSM. Modulation of morphogenesis by noncanonical Wnt signaling requires ATF/ CREB family-mediated transcriptional activation of TGFbeta2. *Nat Genet* 2007;**39**: 1225–1234.
61. Yu H, Smallwood PM, Wang Y, Vidaltamayo R, Reed R, Nathans J. Frizzled 1 and frizzled 2 genes function in palate, ventricular septum and neural tube closure: general implications for tissue fusion processes. *Development* 2010;**137**:3707–3717.
62. Yu H, Ye X, Guo N, Nathans J. Frizzled 2 and frizzled 7 function redundantly in convergent extension and closure of the ventricular septum and palate: evidence for a network of interacting genes. *Development* 2012;**139**:4383–4394.